Near Surface Geophysics

EAGE
EUROPEAN
ASSOCIATION OF
GEOSCIENTISTS &
ENGINEERS

Near-surface three-dimensional multicomponent source and receiver S-wave survey in the Tannwald Basin, Germany: Acquisition and data processing

Thomas Burschil[1,2]*, Hermann Buness[1] and Cedric Schmelzbach[3]

[1]*Leibniz Institute for Applied Geophysics, Stilleweg 2, 30655, Hannover, Germany,* [2]*now at Federal Institute for Geosciences and Natural Resources, Stilleweg 2, 30655, Hannover, Germany, and* [3]*ETH Zurich, Institute of Geophysics, D-ERDW, Sonneggstr. 5, Zurich, 8092, Switzerland*

ABSTRACT

Shallow 3-D reflection seismic surveys using S-waves have rarely been carried out, even though S-waves can provide higher resolution subsurface images than P-waves. We conducted a 3-D near-surface multicomponent source and receiver survey in Quaternary sediments. We employed a small electrodynamic seismic source with a horizontal shaking unit operated in two orientations. Three-component geophones in an orthogonal layout covering an area of 117×99 m^2 were used for recording. Changes in weather and ground conditions, including freezing and thawing during acquisition, directly influenced the data quality and resulted in discernible relative time shifts in the data. Our seismic processing flow included a four-component rotation of the data from the Cartesian acquisition geometry into the 'natural' coordinate frame to orient sources and receivers in radial or transverse orientation to separate different S-wave polarizations. The rotation increased the signal strength and helped, for example, to improve the quality of the images of the basin base. The irregular offset distribution in the common midpoint gathers impedes filtering to suppress surface waves in the *f–k* domain. We, therefore, applied a common-reflection surface processing flow. After regularization, we could better remove the energy of the surface waves. Both stacked 3-D S-wave volumes of vertical and horizontal polarizations provide images of the Quaternary overdeepened Tannwald Basin that was partly known from previous P- and S-wave 2-D surveys. Compared to a P-wave profile adjacent to the volume, however, the S-wave volumes provide higher resolution images of the basin base and internal structure. The basin base is well mapped in three dimensions and shows undulations that were not obvious from the P-wave data. Comparing the S-wave volumes of different polarizations, we find only minor differences in the stacks and interpretations.

Key words: 3-D, data acquisition, data processing, reflection, S-wave.

INTRODUCTION

High-resolution seismic reflection imaging is a well-established tool to study the structure and physical parameters of highly heterogeneous near-surface material, such as Quaternary sediments. Typically, P-wave images derived from

*Email: thomas.burschil@bgr.de

vertical-component source and vertical-component receiver data have been employed to investigate glacial structures to depths of several hundred metres with a vertical resolution of a few to several metres (Büker et al., 1998; Buness, 2007; Pugin *et al.*, 2009, 2013; Burschil *et al.*, 2018, 2019). In the last decades, paralleling the application in the exploration industry (e.g., Hardage *et al.*, 2011), the application of S-wave imaging has become popular for near-surface studies (e.g., Inazaki, 2004; Pugin *et al.*, 2009; Lang *et al.*, 2012; Krawczyk *et al.*, 2013; Brodic *et al.*, 2018). S-waves are characterized by particles oscillating perpendicular to the direction of wave propagation and, thus, can be split in two independent polarizations. Most commonly, these are vertical (SV) and horizontal (SH) polarizations. In comparison to imaging with P-waves, S-waves provide a higher resolution at the same frequency due to much lower S-wave velocities; v_P/v_S ratios can yield values of up to 10 in the unconsolidated near-surface region (Pugin *et al.*, 2013). Thus, it is possible to image shallower reflectors, and one may depict reflections in areas where P-wave surveying is unable to provide crisp images (Burschil and Buness, 2020; Pugin *et al.*, 2013). Furthermore, S-wave surveying can use shorter offsets for reflection imaging than P-waves to cover the same target depth. Whereas the reflection information from the faster P-waves is extracted mainly from outside the cone of surface waves (i.e., from within the so-called 'optimum window' for reflection imaging; Hunter *et al.*, 1984), information from the slower S-wave reflections is derived mainly from inside this cone, and effective surface-wave suppression is important for successful S-wave imaging.

In areas with highly heterogeneous structures, 3-dimensional (3-D) seismic imaging is required to properly resolve the geometry of the subsurface. Whereas 3-D imaging is a well-established tool for seismic exploration of mineral and hydrocarbon resources, 3-D surveying is far from being standard in near-surface applications. This lack of near-surface 3-D surveys is first of all a matter of the different economic interests in different exploration types. In contrast to 2-D surveying, 3-D campaigns are significantly more expensive and hence often economically not attractive to image near-surface targets (Frei *et al.*, 2021). Spatial sampling is one of the main cost drivers of shallow-target seismic imaging. Seismic signals in near-surface surveys are broadband and extend to high frequencies to image details in the shallow subsurface. Properly recording high-frequency signals requires both a dense shot and geophone spacing to avoid spatial aliasing and to image shallow reflectors, and – of importance for 3-D imaging – the source and receiver line separation has to be short

as well. For instance, Büker et al. (2000) required more than 12 000 shots and 85 days of acquisition time to cover an area of 320×420 m^2 with the goal to image glacial sediments at 15–170 m depth. Thus, 3-D near-surface imaging is relatively rare (House *et al.*, 1996; Bachrach and Nur, 1998; Spitzer *et al.*, 2003; Mari and Porel, 2008; Schmelzbach *et al.*, 2007; Sargent and Goulty, 2007; Sloan *et al.*, 2009; Kaiser *et al.*, 2011; Lundberg *et al.*, 2014).

The use of S-waves in 3-D seismic exploration is nowadays almost exclusively limited to analysing converted waves using conventional vertical-component sources and three-component (3-C) receivers (P-to-SV conversions; e.g., Garotta, 1999; Chopra and Stewart, 2010; Hardage *et al.*, 2011, 2014; Donati *et al.*, 2016). Pure S-wave surveys employing horizontally oriented sources and receivers (1-C, 2-C or 3-C sources and 2-C or 3-C receivers) are very rare (Potters *et al.*, 1999; Simmons *et al.*, 1999; Davogustto Cataldo *et al.*, 2014). The latter ones face a series of problems: (1) the excitation of S-waves with horizontally oriented forces is more intricate than for conventional vertically-oriented forces (Simmons and Backus, 1999a); (2) a pure single-mode excitation of waves is not possible (Pugin and Yilmaz, 2017), since any real source excites SH- as well as SV- and P-waves in different angles and azimuths; and (3) anisotropy leads to S-wave splitting (Alford, 1986; Crampin, 1985; Simmons and Backus, 1999b), demanding an elaborate processing to properly treat the different S-wave modes. Nonetheless, 9-C seismic methods are used in the in the industry to image deeper targets (e.g., Shuck *et al.*, 1996; Hitchings and Potters, 2000; Davis *et al.*, 2003; Clochard *et al.*, 2018). Pan *et al.* (2021) used a random objective wave function approach to evaluate a shallow 3-D 9-C experiment by full-waveform inversion, but did not perform reflection imaging. Considering seismic imaging of the near-surface region, there are, to the best of our knowledge, no published reports on 3-D multicomponent seismic reflection surveys.

However, we expect the benefits of 2-D S-wave imaging also for 3-D. For the study presented here, the objectives of our small-scale 3-D S-wave survey using 6-C data (two horizontally oriented source components recorded by 3-C geophones) were (1) to demonstrate the feasibility of shallow 3-D multicomponent S-wave surveying, (2) to map the sedimentary succession of an overdeepened Quaternary valley in high detail, and (3) to explore the presence of anisotropy. In this paper, we present the first 3-D S-wave reflection seismic dataset recorded in a glacially overdeepened Quaternary basin, with our survey being located in the Tannwald Basin, situated in the Alpine foreland (Fig. 1a). The scope of this paper comprises
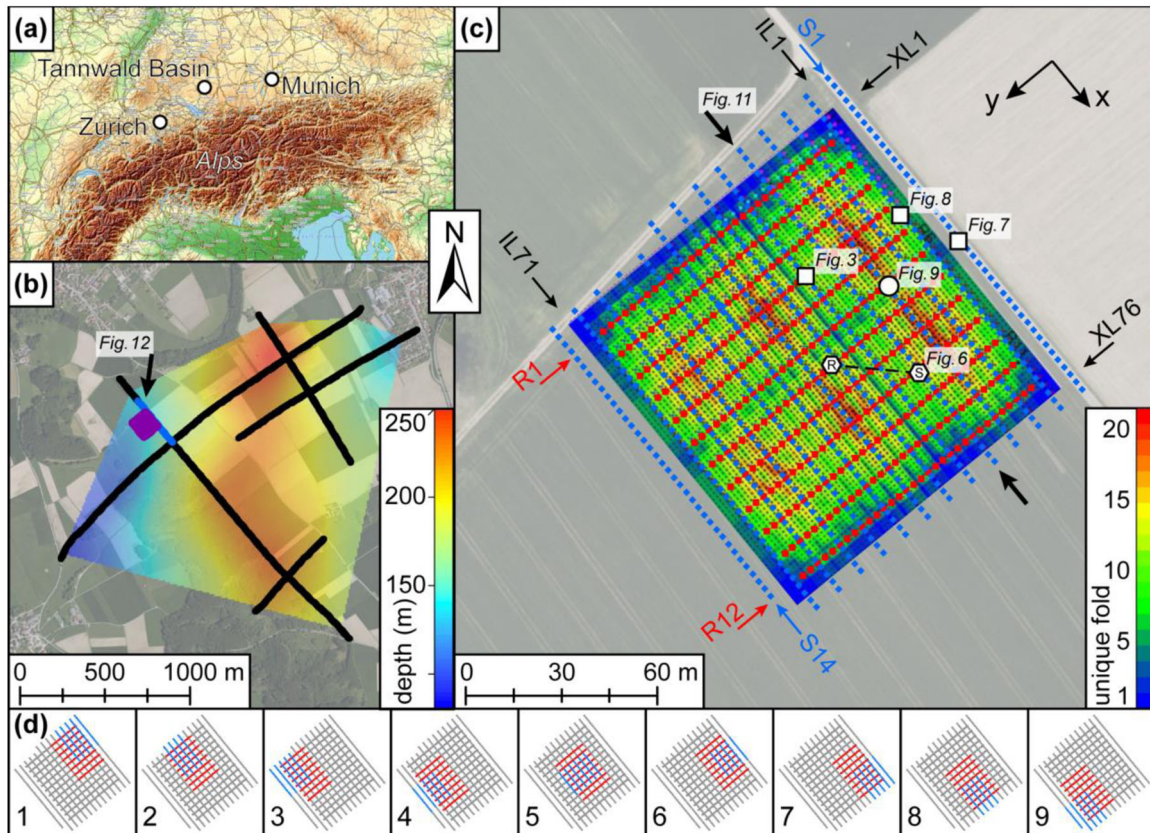
Figure 1 (a) Overview showing the location of the Tannwald Basin in the Northern Alpine foreland. (b) Aerial photo of the Tannwald Basin with 3-D area (purple), seismic profiles (black lines), location of a prior acquired P-wave profile for comparison (blue line), and depth of the basin base (modified after Burschil *et al.*, 2018). (c) Acquisition geometry with source positions (blue rhombi) in source lines S1–S14, receiver positions (red squares) in receiver lines R1–R12, as well as unique fold of CMP in inlines IL1–IL71 and crosslines XL1–XL76. (d) Patch configurations 1–9 of sources (blue), live receivers (red) and inactive sources and receivers (grey). Labels (Fig. x) show the source, source–receiver pair and line locations presented in this paper. Source: OpenTopoMap, BKG 2020

a discussion of our considerations of acquisition design, data quality evaluation, and strategy for S-wave processing of 3-D 6-C data. The key steps of our 6-C processing strategy are the transformation of the multicomponent data from the acquisition coordinate frame to its natural coordinate frame, and the regularization of the data. Finally, we interpret the 3-D volume in the light of other available seismic and geological data.

GEOLOGICAL TARGET

Glacially overdeepened basins are subglacially formed troughs that were excavated deeper than the fluvial level into the landscape during the glaciation period (Cook and Swift, 2012). Glacial, fluvial, and lacustrine deposits subsequently filled these troughs and are preserved as sedimentary archives. Due to rapid change in the depositional environment during the filling, the sediments are often spatially

varying. The sedimentary records also contain information about the depositional environment and, thus, about climatic history (Buechi, 2017). To reveal this history is the aim of the project 'Drilling Overdeepened Alpine Valleys' (DOVE; Anselmetti *et al.*, 2016), funded by the International Continental Scientific Drilling Program. The Tannwald Basin (TB) is an overdeepened basin and one of the DOVE drill sites. It is located in Southern Germany, about 50 km north of Lake Constance in the Alpine foreland.

Prior to the DOVE drilling operations in the TB, a net of high-resolution 2-D seismic profiles, interpreted using the stratigraphy of a cored research borehole, revealed the shape and the infill of a 250-m-deep overdeepened basin (Fig. 1b; Burschil *et al.*, 2018). Further S-wave surveys (Burschil and Buness, 2020) and a 3-D investigated area with P- and S-waves (Buness *et al.*, 2020) complement the seismic investigations so far. The TB is cut into Tertiary Freshwater Molasse and

Table 1 Acquisition details and geometry. $\vec{x}$, $\vec{y}$, and $\vec{z}$ refers to the direction of the Cartesian acquisition coordinate system (see Fig. 1)

# source lines ($\vec{x}$) / # receiver lines ($\vec{y}$) / # patches	14 / 12 / 9
Point / line spacing	3 m / 9 m
# CMP / CMP bin size	5396 / 1.5 m×1.5 m
Inlines ($\vec{x}$) / crosslines ($\vec{y}$)	71 / 76
max (unique) CMP fold	76 (21)
Source (peak force)	ELVIS-VII (1 kN)
# source points / excitation	598 / 2x $\vec{x}$, 2x $\vec{y}$
Source signal / duration / frequency range	linear sweep / 12 s / 20–100 Hz
Receivers	3-C geophones ($\vec{x}/\vec{y}/\vec{z}$)
Geophone type, resonance frequency	SM-6, 14 Hz
# geophones / # receiver positions / # channels	128 / 384 / 384
Seismographs /# seismographs	Geometrics Geode /16
Recording / listening time / sampling interval	uncorrelated / 14 s / 2 ms

Upper Marine Molasse (Ellwanger *et al.*, 2011). The sedimentary succession of the Quaternary basin comprises, from bottom to top, (1) sheared allochthonous molasse, (2) waterlain till, (3) a thick package of fine-grained basin fines that transits into a coarsening-up sequence in the upper part, followed by (4) upper till and sand layers. The uppermost layer consists of (5) fluvial sand and gravels of the outwash plain of the last glaciation.

SURVEY DESCRIPTION

In February 2018, we carried out a 3-D survey using a 2-C source (two horizontal components) and 3-C receivers for S-wave imaging in the Tannwald Basin (TB) (Table 1). In favour of a symmetrical sampling (e.g., Vermeer, 2010), we choose a rectangular acquisition geometry with equal source and receiver line spacing and equal point spacing for sources and receivers along the lines. Our survey-design requirements were (1) an investigation depth >140 m to image the basin base, (2) aliasing-free imaging and (3) an investigated area ≥100×100 m² to be able to interpret areal horizons. Further constraints were (4) limited time and (5) the available equipment.

Our most important survey-design considerations were:

1. During the previous surveys (Burschil *et al.*, 2021), we conducted source tests that showed that the small electrodynamic micro-vibrator ELVIS-VII (Polom *et al.*, 2011, 2018) with 1 kN peak force provides sufficient energy to generate detectable reflections from 200 m depth in this area. The wheelbarrow-mounted ELVIS source is also small enough to be operated effectively on farmland without field damage. Furthermore, our source tests showed that frequencies up to 100 Hz could be injected into the ground as well as recorded at the maximum offsets of interest (<100 m).

2. To avoid spatial aliasing, the bin size b for common midpoints (CMP) can be calculated with:

$$b \leq v_{RMS} / \left(4 f_{max} \sin \alpha \right) \tag{1}$$

(Cordsen *et al.*, 2000). From previous surveys, we estimate a near-surface stacking velocity to be $v_{RMS} > 400$ m/s. With a maximum frequency $f_{max} = 100$ Hz of the sweep and $\alpha = 30°$, the bin size has to be smaller than 2 m. We chose a conservative value of $b = 1.5$ m, which results in a source-receiver point spacing of 3 m (Table 1).

3. We chose a source and receiver line spacing of 9 m. This line spacing defines the fold and shallowest resolvable reflectors. The shallowest mappable reflector is about 1.0–1.2 times the line spacing (Cordsen *et al.*, 2000). Our line and point spacing results in 14 source lines (598 source positions) and 12 receiver lines (384 receiver positions) that are oriented perpendicular to the source lines (Fig. 1c).

4. To conduct the survey within a reasonable time, we limited the number of source positions. Since small offsets (<60 m) are sufficient for S-wave reflection imaging (Burschil and Buness, 2020), active source positions were restricted to be located within the patch of the active receivers only (Fig. 1d).

5. With our equipment of 128 3-C geophones, we split the whole survey area into nine patches. We simultaneously measured eight active receiver lines with 16 geophones each, while activating the source along four to six source lines (Fig. 1d). We paid attention that the unique fold, i.e. the number of filled offset bins of 3 m length, is not below 10 for most of the area.

Given these survey-design prerequisites, a crew of four people conducted the survey in a total of ten days, including two days of installation and eight days of operation. The surveyed area was located on the ploughed cropland (Fig. 2). Source and receiver components were oriented in parallel or consistent orthogonal orientations (according to
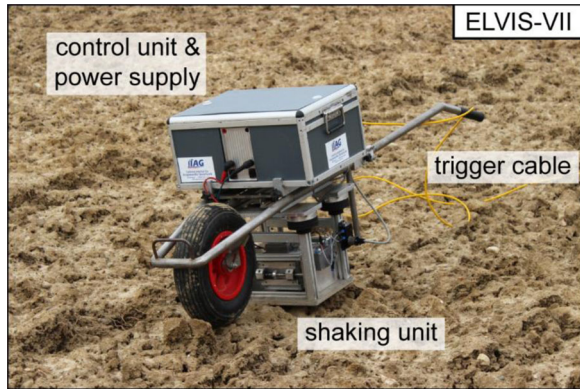
Figure 2 Wheelbarrow-mounted electrodynamic source ELVIS-VII. Photo: D.C. Tanner (LIAG)

Hardage *et al.*, 2011) with respect to an acquisition *x–y* reference coordinate system (Fig. 1c). Source lines run parallel to the *x*-direction while receiver lines were oriented parallel to the *y*-direction. The seismic source was the vibrator ELVIS-VII (Fig. 2). The horizontal shaking unit excited two sweeps of opposite polarization in both the *x*- and *y*-directions. The source signal was a linear sweep ranging in frequencies from 20 Hz to 100 Hz for a duration of 12 s. Sixteen Geometrics Geode seismographs recorded the ground motion at 128 3-C geophones with the geophone components being oriented in the *x–y*-z direction.

DATA QUALITY AND WEATHER INFLUENCES ON THE SEISMIC DATA

Two horizontal source orientations (*Sx* and *Sy*) and 3-C receivers (*Rx, Ry* and *Rz*) result in one 6-C data set for each source position. In the unprocessed source gathers (Fig. 3), cross-correlated with the pilot sweep, i.e. the recorded synthetic sweep of the sweep generator, we identify a strong reflection at 600 ms two-way traveltime (green arrows), which is most distinct on parallel source and receiver components (*SxRx, SyRy*). This reflection is visible also on orthogonal horizontal components (*SyRx, SxRy*), but rather faint on vertical receiver components (*SxRz, SyRz*; red arrows). Furthermore, all recordings show near-offset, source generated noise, likely caused by clipped geophones (orange arrows) and surface waves are observed for some components (blue arrow).

Weather and ground conditions significantly changed during the survey as illustrated by the temperature and precipitation data observed at the nearest meteorological station (Fig. 4). Changing temperatures and snowfall in the night

on 8 February caused freezing and thawing of the soil of the farmland. These changing weather conditions left a discernible imprint in the seismic data. For example, the first arrivals show time shifts depending on the day of operation. These are most significant for patches 1 and 9 (blue arrows in Fig. 4). Temperature T_{max} dropped after the first operation day and T_{min} was significantly lower on the night before measuring patch 9. Temperature changes during the day result in a minor time shift that we observe for the first arrivals of patches 6 and 7 (orange arrow in Fig. 4). We assign these traveltime changes to weather-dependent ground conditions and resultant S-wave velocity changes in the shallowest subsurface.

SEISMIC DATA PROCESSING

For data processing, we followed the tailored S-wave processing scheme to highlight small-scale structures, presented by Burschil and Buness (2020). We adapted the processing workflow regarding the 3-D nature of the survey and the irregular offset trace distribution (Table 2).

Component rotation

A key processing step was component rotation. In 2-D S-wave profiling, the excitation direction of a horizontally oriented source is commonly chosen to be either parallel or perpendicular to the profile direction to excite and record pure SV- or SH-waves, respectively, assuming a 1-D and isotropic subsurface. However, the azimuthal direction between source and receiver varies for each source–receiver pair in a 3-D survey (Simmons and Backus, 1999a). To process SV- and SH-waves, we, therefore, rotated the horizontal components from the acquisition geometry with inline–crossline components *x* and *y* into radial–transverse orientations *r* and *t*. For this trigonometric projection, we acquired four horizontal directions of the ground motion per source–receiver pair (Fig. 5). Alford (1986) and DiSiena *et al.* (1984) introduced the methodology to transform data from an *x–y* oriented geometry (blue in Fig. 5) into a cylindrical *r–t* coordinate system (green in Fig. 5; Hardage *et al.*, 2011; Schmelzbach *et al.*, 2016).

$$\begin{bmatrix} SrRr & StRr \\ SrRt & StRt \end{bmatrix} = \begin{bmatrix} \cos\theta & -\sin\theta \\ \sin\theta & \cos\theta \end{bmatrix} \begin{bmatrix} SxRx & SyRx \\ SxRy & SyRy \end{bmatrix} \begin{bmatrix} \cos\theta & \sin\theta \\ -\sin\theta & \cos\theta \end{bmatrix}. \quad (2)$$

Four horizontal traces of the source–receiver pair in inline–crossline orientation (*SxRx, SxRy, SyRx, SyRy*) are projected onto radial–transverse components (*SrRr, SrRt, StRr,*
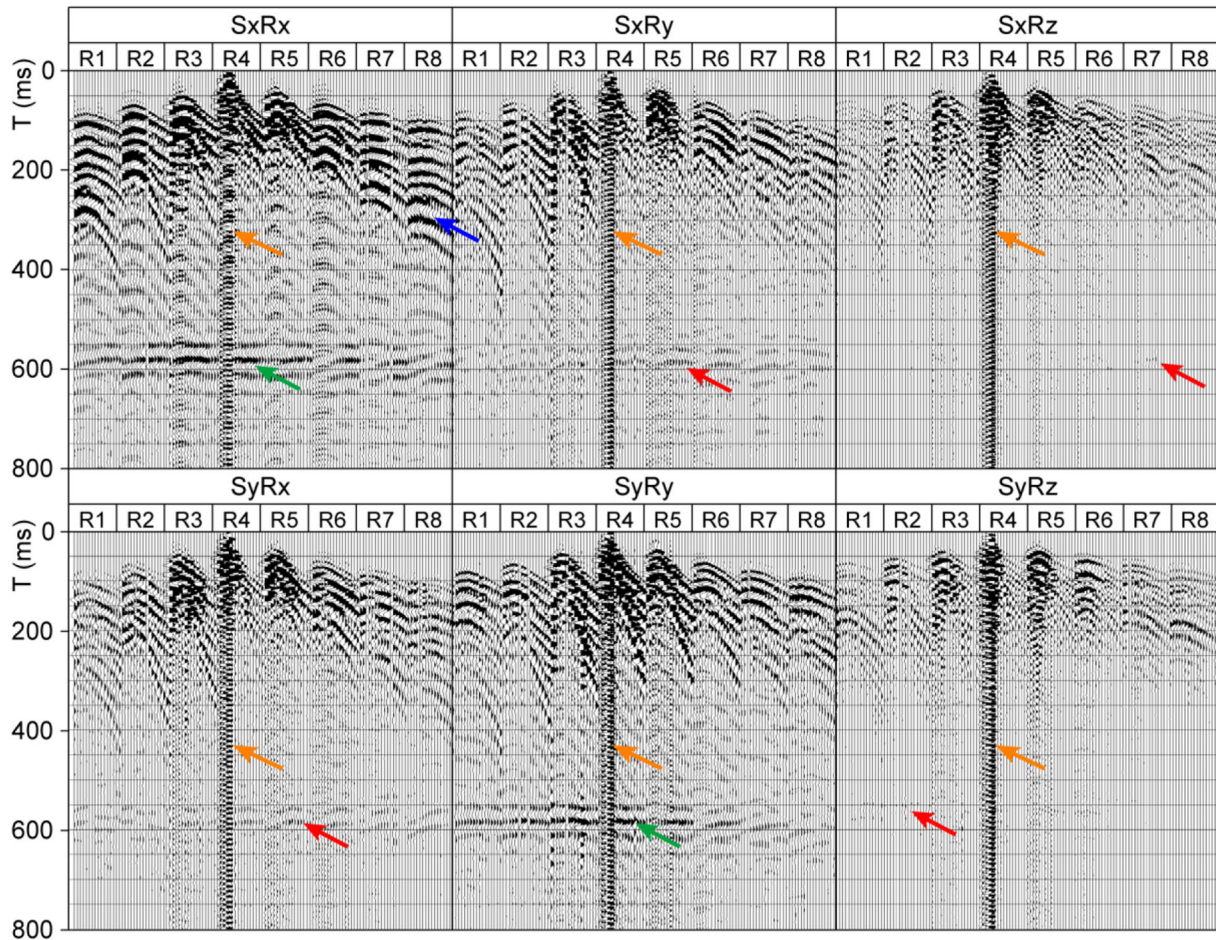
Figure 3 Acquired 6-C data in the *x–y–z* acquisition coordinate system for source location 231 and receiver lines R1–R8 (see Fig. 1c). Gathers are sorted according to source directions *Sx* and *Sy*, and receiver directions *Rx, Ry* and *Rz*. The traces are normalized, and a power time gain is applied. Arrows highlight features discussed in the text

StRt) by applying rotation matrices containing the source–receiver azimuth θ.

During field operations, we rotated the source by lifting and setting it at the same position. To compensate for varying source coupling for both excitation directions at the same source location, we balanced each source gather according to its maximum amplitude and rotated the horizontal components geometrically using the azimuth of each source–receiver pair (Eq. 2). The unrotated data show a complex and unfocused horizontal particle oscillation in the *Rx–Ry* view. Component rotation projects the ground motion onto parallel source–receiver components and lets us distinguish between SV-wave on the *SrRr* component (green line in Fig. 6) and SH-wave on the *StRt* component (purple line in Fig. 6) for both surface waves and reflections.

Source gathers of the unrotated data show seismic energy on all four horizontal components, clearly visible for the 600 ms reflection (Fig. 7). Component rotation focuses energy on the two parallel components *SrRr* and *StRt* (green arrows) in the radial–transverse coordinate system. However, not all energy is projected onto the *SrRr* and *StRt* components, and a faint remnant of the reflection is still present on the orthogonal components (orange arrows). Furthermore, the component rotation makes the surface waves appear more distinct on the *SrRr* and *StRt* components (blue arrows), whereas they are spread over all recordings in the acquisition coordinate system.

Surface waves become distinguishable on the parallel components. The *SrRr* component shows Rayleigh surface-wave arrivals, while the *StRt* component shows the Love
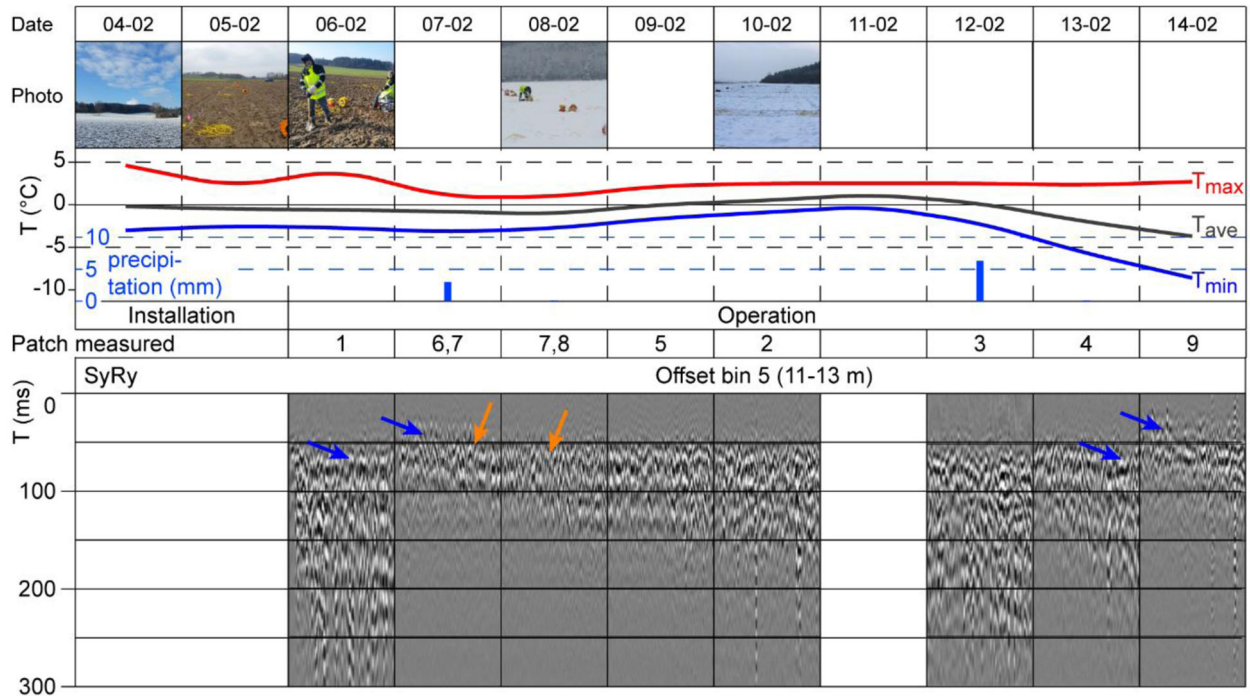
Figure 4 Weather conditions during the survey in February 2018. Daily temperature and precipitation data from nearest meteorological station Weingarten, Kr. Ravensburg, about 23 km southwest of the study site (Source: https://cdc.dwd.de/portal/; source: DWD). Offset bin gather for source–receiver component *SyRy* in chronological order. Traces are normalized. Blue arrows mark features discussed in the text. Photos: H. Buness, D.C. Tanner, V. Kipke (LIAG)
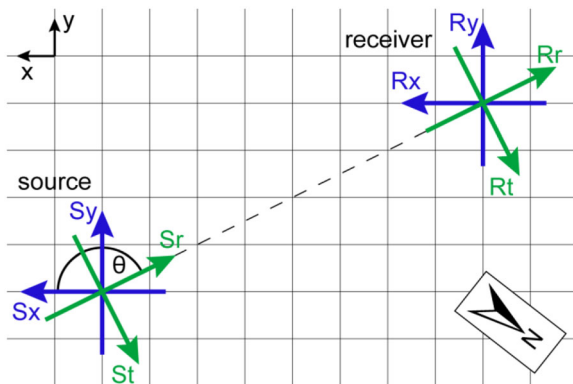

Figure 5 Rotation of horizontal source (S) and receiver (R) components (top view) by the source–receiver azimuth θ from the *x–y* acquisition coordinate system (green) into the radial–transverse coordinate system (blue), illustrated with one example source–receiver pair. Both coordinate frames are right-handed with the vertical axis pointing downwards. The north arrow indicates the orientation of the acquisition grid (see Fig. 1). Figure modified after Hardage *et al.* (2011)

surface wave (blue arrows in Fig. 7). Hodograms of the particle motion also depict the oscillations of both types of surface waves. The Rayleigh surface-wave velocity is

$v_{Rayleigh} = 320$ m/s and Love surface-wave velocity slightly higher $v_{Love} = 340$ m/s. This conforms with the theoretical values, where $0.9\ v_S \lesssim v_{Rayleigh} \lesssim 0.95\ v_S$ and is between the shallow and deep S-wave velocities of the $v_{shallow} < v_{Love} < v_{deep}$ (Sheriff and Geldart, 1995).

For amplitude scaling, we applied a spherical divergence correction with a constant velocity of 500 m/s and a multiplication with a time-dependent factor t^1 (Fig. 8). This is necessary to conserve the relative amplitudes and ensure comparability of amplitudes between the different components. A trace equalization process normalized the amplitudes of each trace to its maximum and balanced the amplitudes of the traces to compensate for the remaining amplitude decay due to the source–receiver offset.

Data regularization and fan filtering

To suppress linear arrivals of refracted and surface waves, Burschil and Buness (2020) applied multi-trace processing, including *f–k* filtering applied to gathers with an equal trace spacing. The offset sorted gathers of the 3-D data show an irregular offset distribution that prevents an effective

Table 2 Processing workflow with steps 1–21, performed in SeisSpace/ProMAX

|		
1	Data import	
2	Vibroseis correlation	With pilot sweep
3	Quality control	Kill noisy traces, check trace polarity
4	Vertical stacking	
5	Assign geometry	
6	Ensemble balancing	
7	Component rotation	Performed in MATLAB
8	Elevation static correction	Final datum 600 m, $v_{replace} = 500$ m/s
9	Residual static correction	Power Autostatics
10	Spherical divergence correction	$v = 500$ m/s
11	Gain correction	Time-power gain t^1
12	Spectral whitening	Frequency band 20–85 Hz
13	Frequency filtering	Band passed 20–100 Hz
14	Trace equalization	
15	Velocity analysis	Initial velocity field for CRS stacking
16	Data regularization by CRS stacking	Bin size: 2 m, Aperture: 0 ms–4 m, 200 ms–5 m
17	Fan filtering (*f–k* domain)	Passing window: >-1000 and $<+500$ m/s for 20–100 Hz
18	Velocity analysis	Velocity field for NMO correction
19	Normal moveout correction	Manually picked top mute
20	Common midpoint stacking	
21	Time-to-depth conversion	With single velocity function
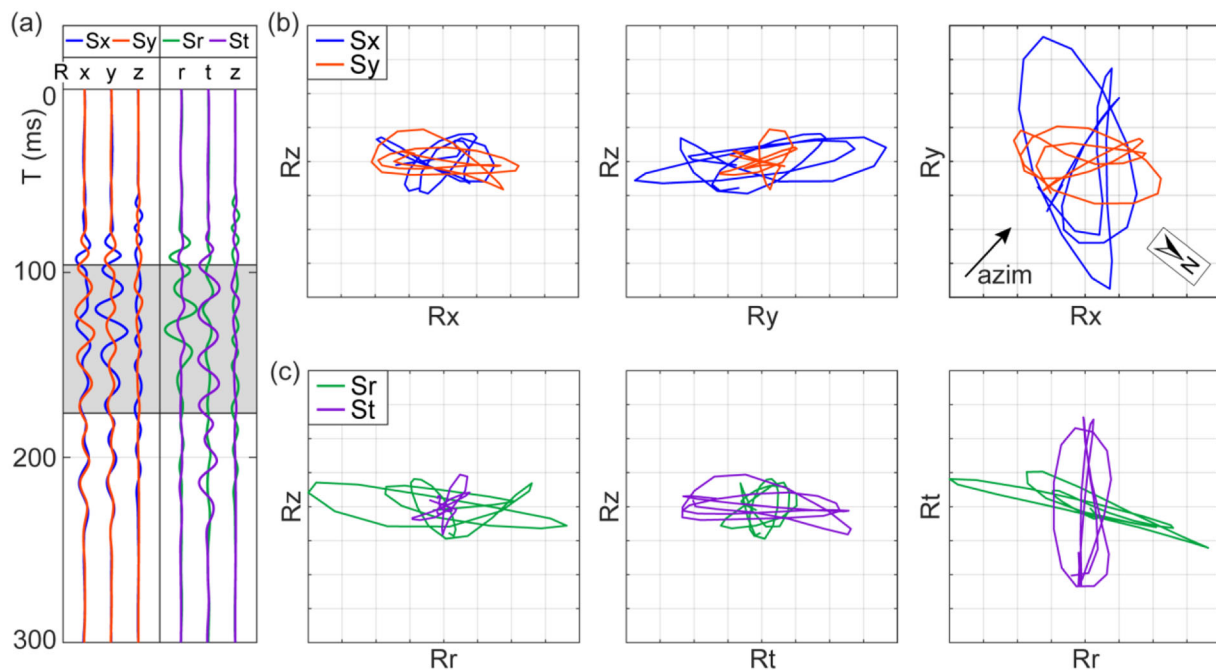
Figure 6 Traces (a) and hodograms before (b) and after component rotation (c) for source–receiver pair (source and receiver locations in Fig. 1c, the time window for hodograms 96–176 ms)

application of the *f–k* filter (orange arrows in Fig. 9a). To enable the attenuation of refracted and surface waves by *f–k* filtering, we regularized the data in order to obtain a regular offset distribution in the CMP domain. We tested two regularization approaches: (1) We combined a number of CMPs into one CMP supergather, binned the data according to the offset, applied differential NMO corrections and stacked the data in each offset bin to one trace per bin. These CMP supergathers then showed a regular offset distribution. (2) We applied common-reflection surface (CRS) processing (Hubral
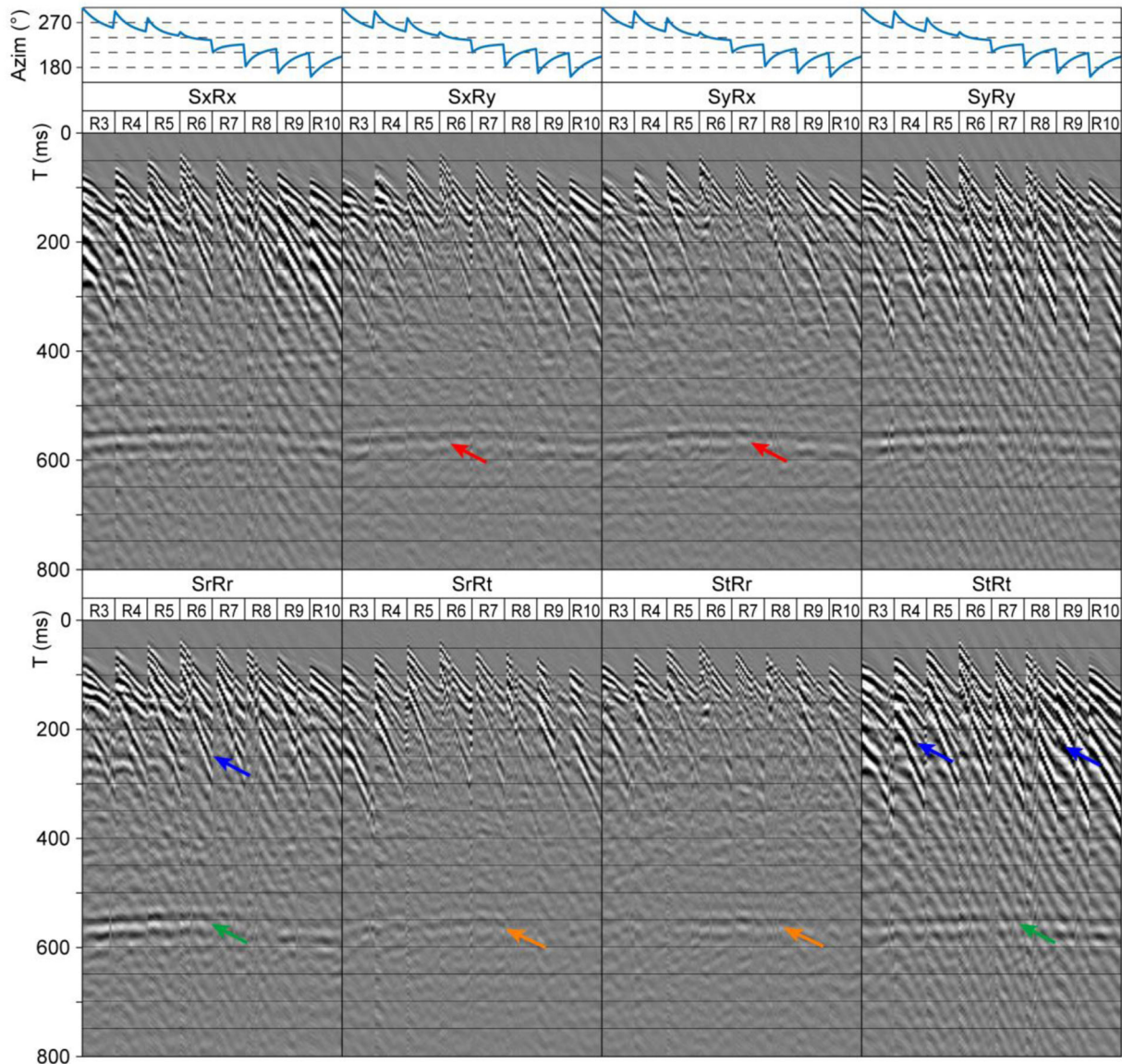
Figure 7 Source gather (see Fig. 1c) showing the four horizontal components for source point 23 before and after component rotation. Each set of four source S and receiver R traces in the *x*–*y* direction is rotated according to the source–receiver azimuth θ into radial (*r*)/transverse (*t*) directions. Gathers are normalized; a power time gain is applied to highlight the 600 ms reflection. Arrows highlight features referred to in the text

et al., 1998) including partial CRS stacking within the offset bins (Gierse *et al.*, 2009). The CRS method aims at sampling contributions from a reflection surface characterized by dip and curvature, which can be determined in a zero-offset stack by coherence analysis. The derived stacking operator is not limited to one CDP, and its aperture can be varied to balance between resolution and signal-to-noise ratio. After regularization, linear arrivals of refracted and surface waves (blue arrows) can now be better recognized in the CRS gathers and the corresponding *f*–*k* domain (blue arrows in Fig. 9).

To remove the linear noise arrivals, we performed filtering in the *f*–*k* domain. After testing different velocity (fan) filters, we rejected areas <-1000 m/s and $>+500$ m/s (red arrow in Fig. 9e). In the filtered CRS gathers, linear onsets are removed and the 600 ms reflection is more clearly visible than before filtering (green arrow in Fig. 9c).
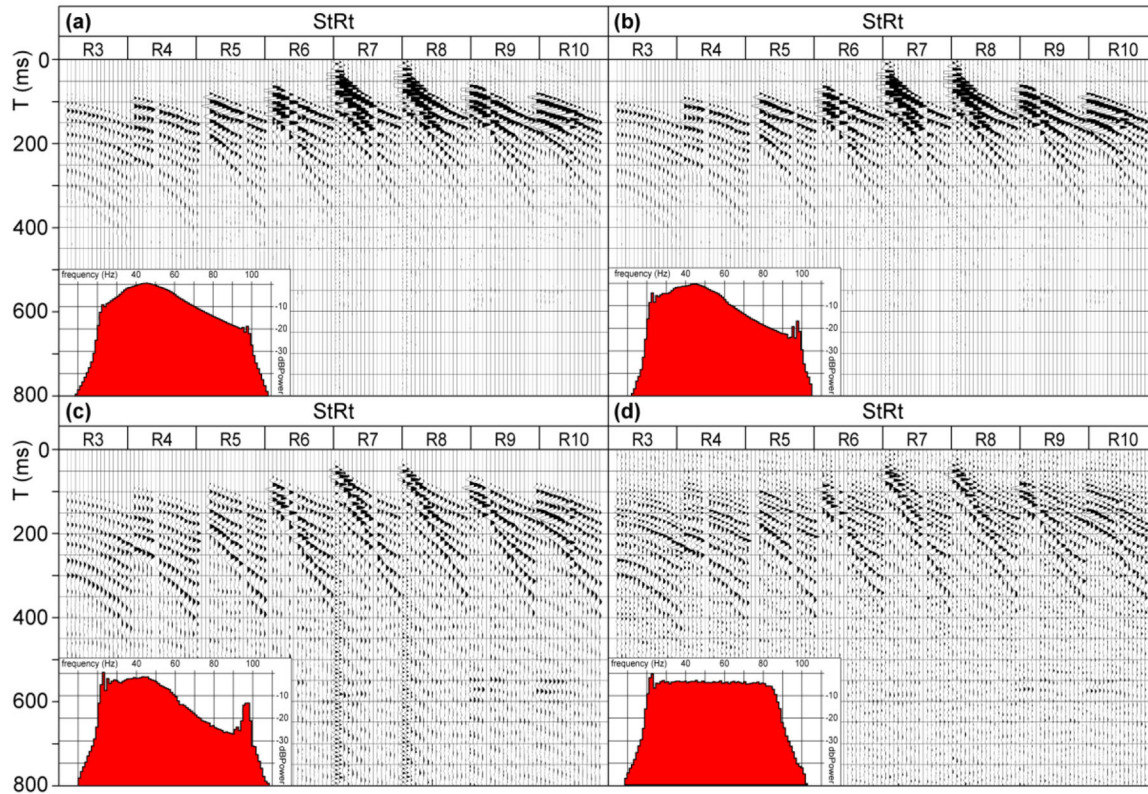
,

Figure 8 Source gathers (see Fig. 1c) and frequency spectra (insets) for the rotated component *StRt* of source location 75 after processing steps 9, residual statics (a); 10, spherical divergence correction (b); 11, time-power gain (c); and 14, trace equalization (d) including 12, spectral whitening (cf. Table 2)

The fan-filtered CRS gathers were subsequently input into several iterations of velocity analysis (Fig. 10). We performed the stacking velocity analysis on *SrRr* and *StRt* components independently to derive two velocity models, one for SV- and one for SH-waves. The two velocity models do not show significant differences considering the picking uncertainty (Fig. 10). Therefore, we used the stacking velocity distribution derived from the *StRt* component for normal moveout corrections of all components. After stacking the NMO-corrected data, we decided to skip the migration of the data volume to avoid edge effects because of the small volume size and the lack of large dips (Fig. 10).

Stacked sections

The most prominent features of the stacked sections are the undulating 600 ms reflection and a reflection package <200 ms visible on the parallel *SrRr* and *StRt* component images (green and purple arrows in Fig. 11). The same reflections

are faint on the *SrRt* and *StRr* component sections (orange arrows). The impact of the changing weather and ground conditions can be seen in the stacked sections as well, in particular for the area of patch 1. The time shift, originally recognized in the first arrivals, results in less coherent and distinct reflections in the <200 ms reflection package (cyan arrows in Fig. 11).

SEISMIC INTERPRETATION

For our interpretation of the S-wave volume, we converted the stacked sections into depth with a single velocity function to compare the interpretation with the interpretation of the nearby recorded P-wave profile (Fig. 12; Burschil *et al.*, 2018). Burschil *et al.* (2018) published five 2-D P-wave seismic reflection profiles. The profiles show a good data quality and were processed using prestack depth migration that resulted in a superior resolution compared to dip-moveout processing and poststack migration. Seismic facies were interpreted on the base of a nearby research borehole. The profiles reveal
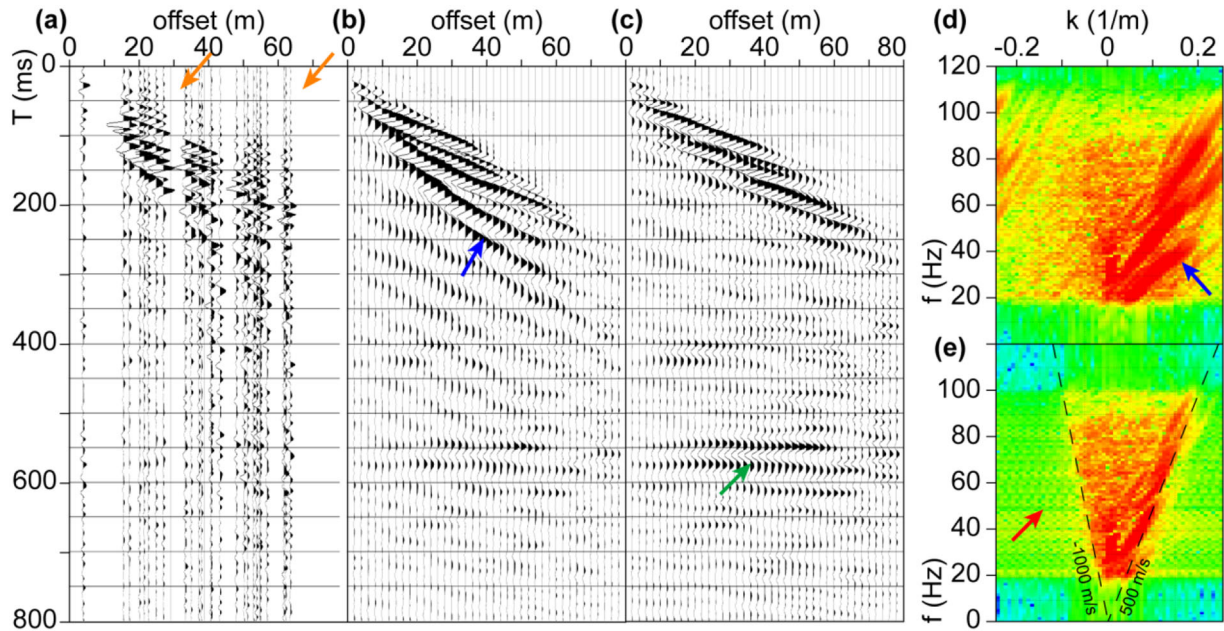
Figure 9 CMP and CRS gathers (see Fig. 1c) of the *StRt* component sorted by offset after processing steps 14, trace equalization, i.e. before regularization (a); 16, data regularization (b); and 17, fan filtering (c). *f–k* spectra for CRS gather without (d) and with (e) fan filter applied. Arrows are referred to in the text

the structure, shape and sedimentary succession of the Tannwald Basin. The displayed profile 3 runs parallel to the inline direction of the 3-D area (Fig. 1b). At the survey location, no other S-wave profiles nor boreholes exist in the surrounding of the 3-D survey to guide the interpretation. The P-wave profile shows a low quality at the location of the S-wave 3-D volume that hampers the joint interpretation. Furthermore, we consider for the interpretation only the SV (*SrRr*) and SH (*StRt*) components and disregard the low-quality patch 1 data (cyan arrows in Figs 11 and 12). 3-D views of the SV- and SH-wave stacked volumes and depth slices are shown in Fig. 13.

From bottom to top, we interpret the observed seismic facies, according to the sedimentary succession described in Section 2, as follows:

Molasse (1) and waterlain till (2) appear as a prominent reflector at around 145–155 m depth (green arrows in Fig. 12). The reflector shows an undulation on both the SV and SH sections, that agree fairly well. The SV section appears even more coherent than the SH section, and both are clearer than the P-wave section. The reflectors correspond to the boundary between the Quaternary sediments on top and the Tertiary Upper Freshwater Molasse below. Possibly, the reflectivity of this boundary is enhanced by the presence of thin units of the waterlain till. The interpreted horizons in SV- and SH-wave

show a great similarity (Figs. 13c, d). The horizon dips eastwards, as expected, since we are at the flank of the valley (cf. Fig. 1b).

The basin fines (3) in 50–130 m depth (blue arrows in Fig. 12) are characterized by relatively faint reflections. Their overall characteristics are discontinuous and weak reflections, but show a similarity between the SV and SH images, even if the two images differ in reflection strength. We took the similarity as a proof that there are faint reflectors within the basin fines, whereas the P-wave section shows no reliable reflections in this region.

The upper till (4) in 20 to 50 m depth (purple arrows in Fig. 12) is dominated by strong low frequency reflections in both sections. Here, we observe a remarkable difference between the SV and the SH section: Layers in the SV section are subhorizontal, whereas reflections are undulating in the SH section. The dip at the right edge of the SH section coincides with the structural dip seen on the P-wave section that shows a vanishing signal just at the edge (magenta arrows in Fig. 12).

The fluvial sand/gravel (5) above 20 m depth shows up with strong straight reflectors in both sections, with the SH section showing higher frequencies. This layer is too shallow to be imaged on the P-wave section.
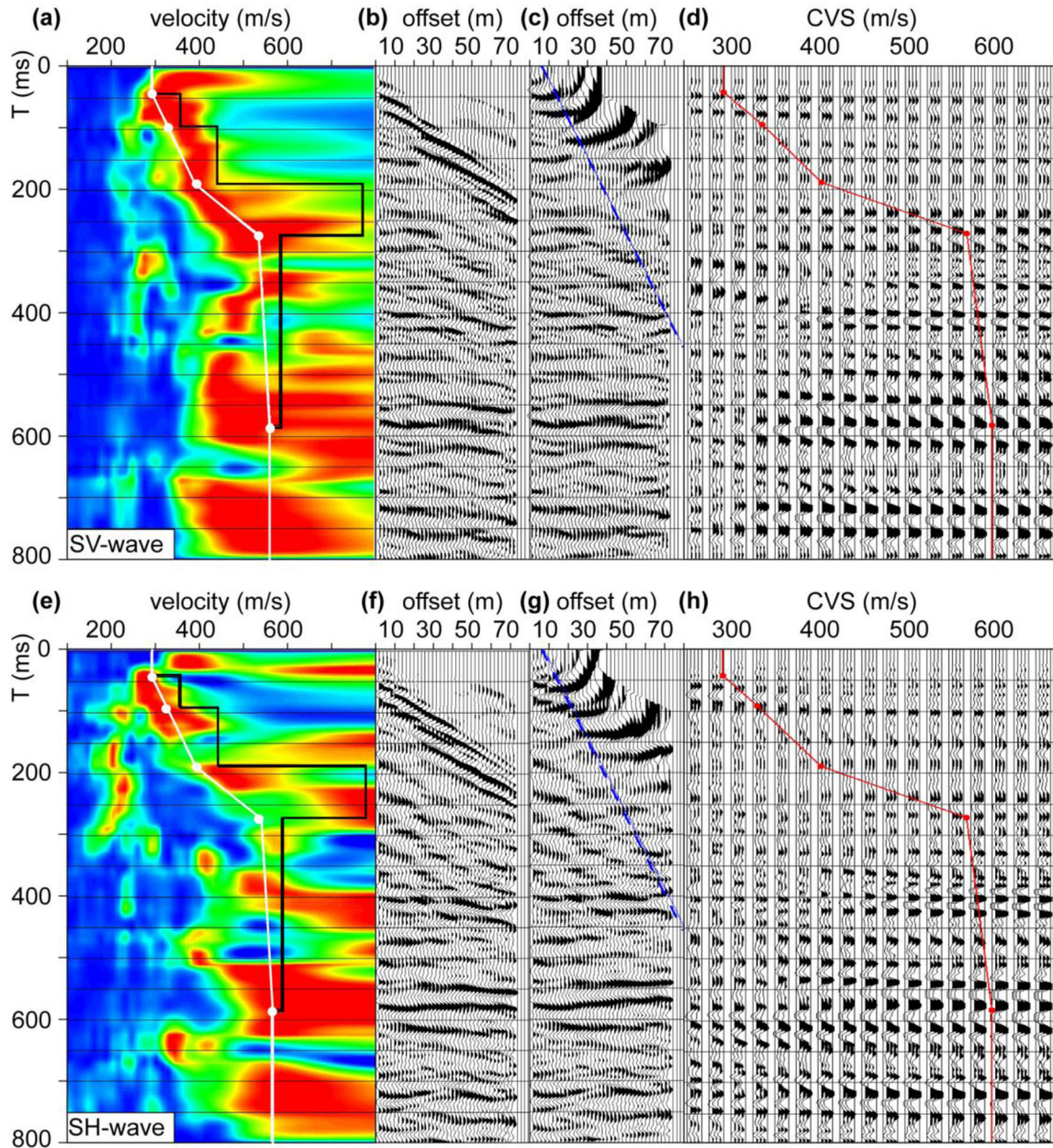
Figure 10 Semblance analysis (a, e) on CRS gather (inline 20/crossline 40), CRS gathers without (b, f) and with (c, g) ith NMO correction applied, and constant velocity stacks (d, h) for (a) SV-wave (a–d) and (b) SH-wave (e–f). Stacking velocity picks and function (white/red dots and lines), interval velocity (black line), and top mute (blue dashed line) after NMO correction

DISCUSSION

Feasibility of shallow 3-D S-wave study

With a moderate effort of time and personnel, we completed a shallow 3-D S-wave survey. However, the efficiency of surveying could likely be improved. The most limiting factor was the number of available channels and/or geophones forcing us to split our survey area into 9 patches. A one-patch solution, requiring 384 3-C Geophones, would save a third of the acquisition time. It would also increase and uniform the fold of offsets (<100 m) of the CMP stacks compared to the fold of the acquired geometry (Fig. 1d).

The small wheelbarrow-mounted source has proven to be sufficient in handling on the ploughed cropland. It would have
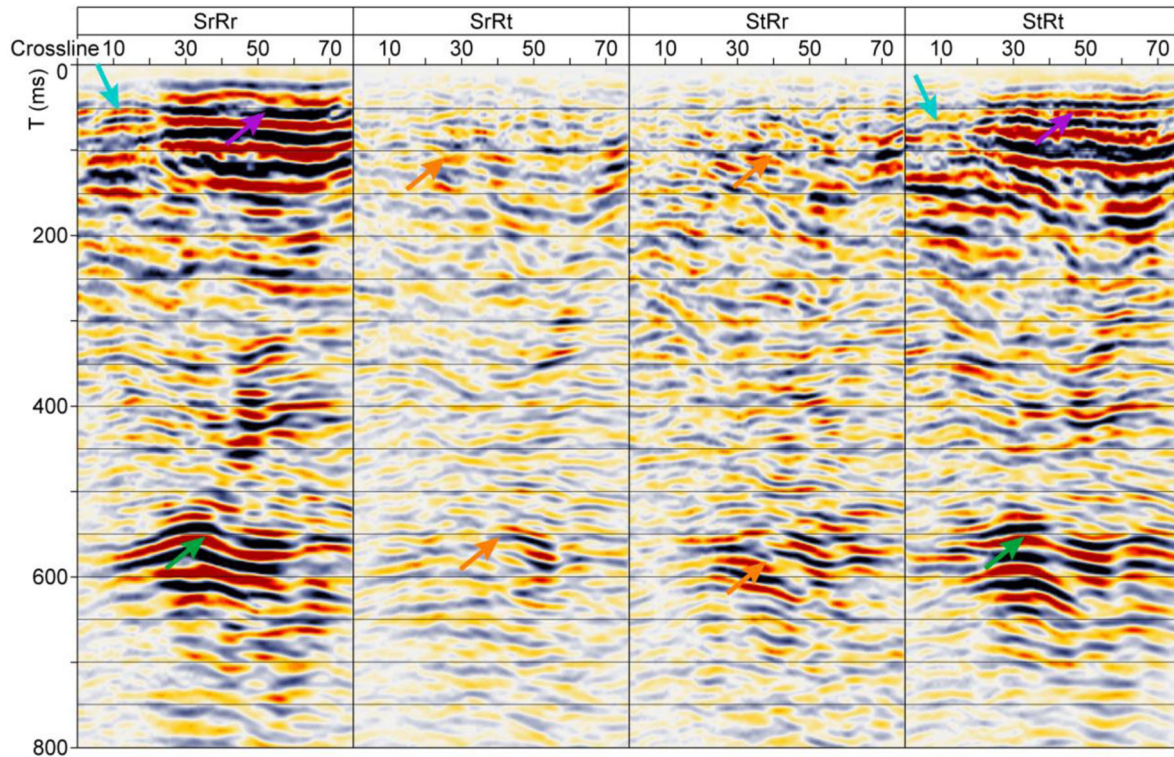
Figure 11 Inline 22 of CRS stacked section for four horizontal components (see, Fig. 1c). Arrows are referred to in the text. The reflection patterns change around crossline 15 due to changing weather conditions at the transition of patch 1 to patch 6

been difficult to conduct these measurements using a heavy vehicle due to accessibility and field damages. The peak force of the vibrator was sufficient to image the deepest parts of the Quaternary sediments at around 140 m depth. The construction of the ELVIS source limits the lowest excited frequency to 20 Hz.

We did not foresee the large influence of the weather conditions on our results (Fig. 4). After recording patch 1 during the first day, the ground conditions changed considerably, which improved the signal quality and source coupling. We were not able to completely correct for the varying signal form and traveltimes, leading to a disruption in the final stack (Fig. 11). For future surveys, we recommend re-measuring the patches that are strongly influenced by changing ground conditions during the survey.

Strategy of S-wave processing

The irregular offset distribution of traces in the CMP gathers of the 3-D volume (Fig. 9a) resulted in problems in seismic processing (Souza *et al.*, 2019), e.g. in filtering the surface waves in the *f–k* domain. To enable multi-trace filtering, we

chose a regularization approach, which is a partial stacking of the data within the offset bins, rather than an interpolation of the data. Therefore, we tested two different approaches. We favoured the CRS processing approach for generating regularized gathers instead of increasing the bin size or using a flex bin approach (Brune *et al.*, 1994; Spitzer *et al.*, 2003), since it is able to respect the dip of the reflectors. In fact, the regularization caused an increase of the stacking fold that improved the signal-to-noise ratio (Eisenberg-Klein *et al.*, 2008) and reflections became more coherent in the CMP gathers (Fig. 9c).

A ringing at the edges of the excited frequencies can be seen in the spectra (Fig. 8). We address a ringing to be an effect of correlation of the sweep with the recorded data that are clipped in the near offset.

Removing the surface waves by fan filtering worked well on the CRS gathers, as previous studies have shown (e.g., Wadas et al., 2016; Brodic *et al.*, 2017; Burschil and Buness, 2020). We tested other approaches, e.g. filtering in the τ-p domain (Schmelzbach *et al.*, 2007), but the applied approach worked best. However, the strong arrivals of refracted and guided waves could not be fully removed, probably due to
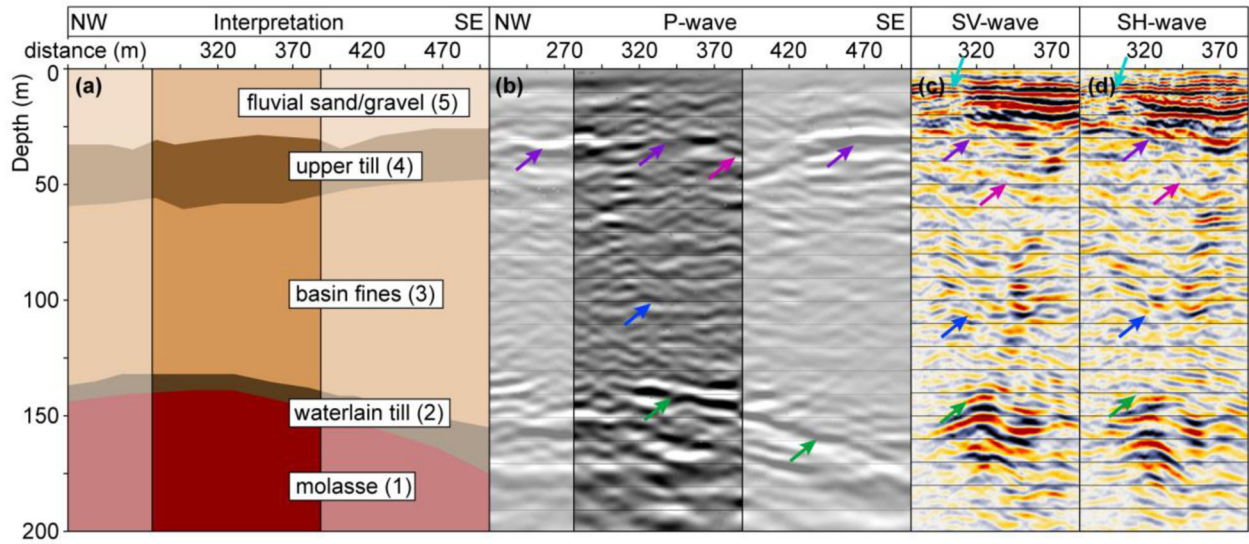
Figure 12 Geological interpretation (a) of the 2-D P-wave prestack depth migration section (b), modified after Burschil *et al.* (2018). Inline 22 of 3-D SV-wave (c) and the SH-wave stacks (d). The P-wave profile and inlines are parallel and about 35 m apart. The position of the P-wave profile (b) is shown in Fig. 1b. The final datum is 580 m. Arrows are referred to in the text

a strong vertical velocity gradient so that different velocities contribute to this wave package. Therefore, we cannot exclude that arrivals of guided and refracted waves contribute to the high reflectivity pattern that we interpret as the upper till layer.

The application of refraction static corrections was not successful since first arrivals were not pickable, which is known for vibratory sources (Yilmaz, 2001), and due to the irregular offset of the acquisition geometry. A decoupled static correction was not considered, since it should (1) be time-dependent that respects the changing weather conditions and (2) respect that various receivers were de-/installed at the same location and active in different patches. Instead, we applied elevation and residual static corrections to the data that were calculated based on the entire dataset.

Component rotation of the raw data that have been acquired in a rectangular layout was necessary to distinguish between vertically and horizontally polarized S-waves (Simmons and Backus, 2001). A rotation to radial–transverse orientations has minor effects on straight 2-D acquisition because a horizontal source is usually aligned parallel and/or orthogonal to the profile direction. The rotation formula is proportional to the cosine of the angle between source and receiver orientation so that small angles have minor effects on component rotation. Nonetheless, polarization analysis and component rotation to radial–transverse components have been performed in 2-D multicomponent studies (Pugin *et al.*, 2009; Schmelzbach *et al.*, 2014; Brodic *et al.*, 2018). For 3-D multicomponent data, the separation of different wave types is

mandatory to analyse the data according to differently polarized S-waves (Pugin and Yilmaz, 2019), for example for the detection of fractures (Davogustto Cataldo *et al.*, 2014; Grossman and Popov, 2014) and surface waves (Pan *et al.*, 2016).

From the sedimentary succession, we assume a horizontal fine-layering in the sediments that would result in polar anisotropy with a vertical symmetry axis (vertical transverse isotropy) that would have minor effects on the data. Most S-wave studies detect anisotropy in a medium with a horizontal symmetry axis (e.g., Alford, 1986; Harris, 1996; Davogustto Cataldo *et al.*, 2014) and can therefore observe shear-wave splitting and detect anisotropy. Velocity analysis of the NMO in the CRS gathers, individually performed for the *SrRr* and the *StRt* components, does not exhibit an unambiguous difference in the seismic velocities (Fig. 10), since the hyperbola moveout is small for the S-wave. Differences are in the range of uncertainty of the semblance analysis. Therefore, we do not infer anisotropy from the presented data.

The reflectors of the till layer (4) show a different reflection signature for SV- and SH-waves and even for the P-waves (Fig. 12). The SV-wave reflectors on the *SrRr* component exhibit a slightly higher dominant frequency compared to the reflectors of the SH-wave on the *StRt* component. Pugin *et al.* (2009) also reported a higher dominant frequency for the SV-wave than for the SH-wave for the same reflector, for multicomponent surveys in Canada. We address the difference in the different reflection coefficients of SV- and SH-waves (Simmons and Backus, 2001). Furthermore, in 3-D surveying,
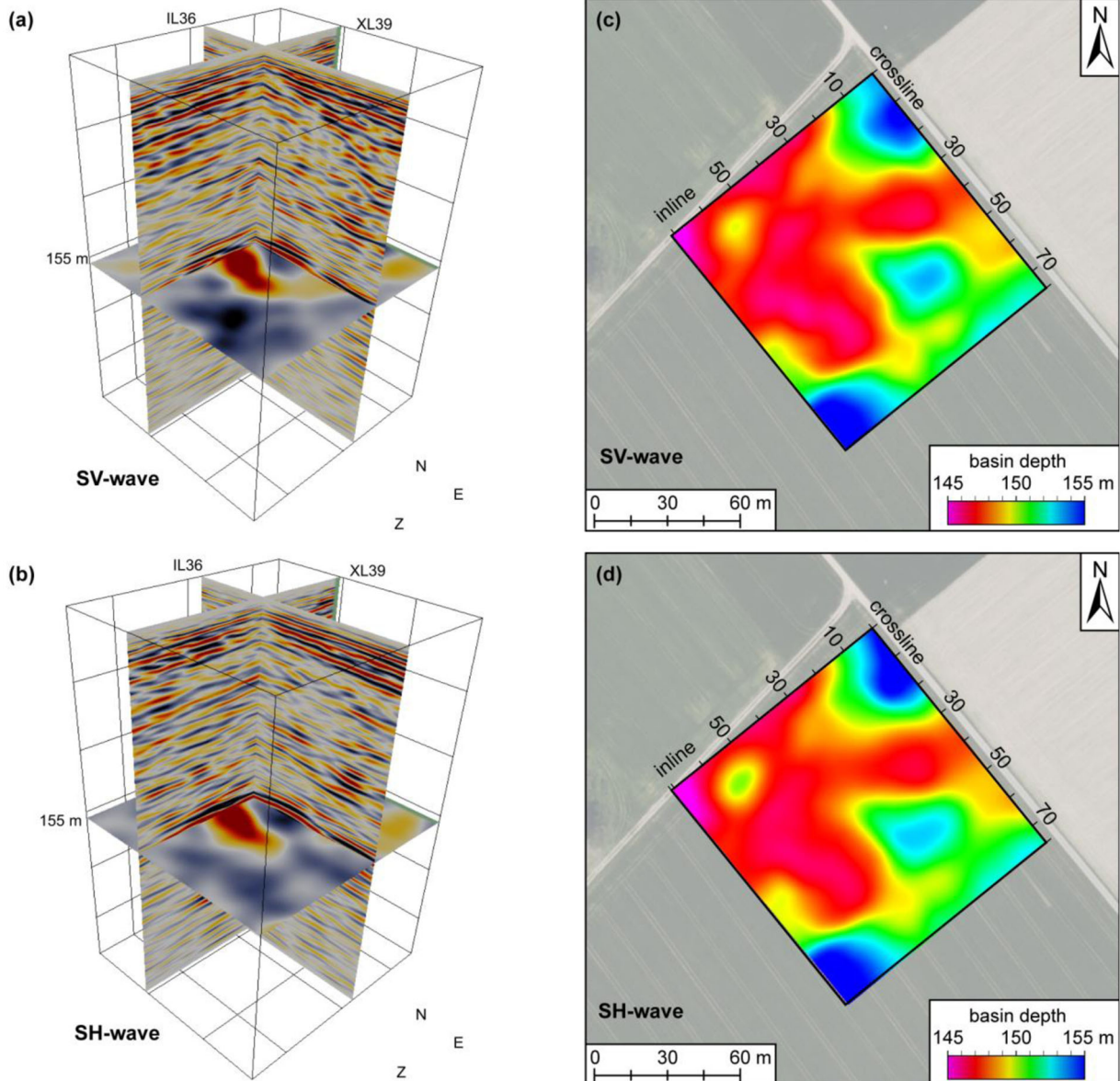
Figure 13 A 3-D view of the volume towards the north for the (a) SV- and (b) SH-wave stacks and depth of the basin base, interpreted from (c) SV- and (d) SH-wave volumes

the horizontal source in the *x*-direction generated an SH-wave in the *x*-direction and an SV-wave in the *y*-direction. We cannot determine a difference in the source coupling. Nonetheless, a different spatial radiation pattern of the wave energy could be a reason for a different reflection signature. A depression at the bottom of the till layer is visible in the SH-wave (magenta arrows in Fig. 12), but not so obvious in the SV-wave. This could be due to superimposed and not completely removed Rayleigh surface waves in the data. A depression is also suggested in the P-wave data.

CONCLUSIONS

We presented the first shallow small-scale 3-D multicomponent source and multicomponent-receiver S-wave investigation, performed in the overdeepened Tannwald Basin. The survey, designed to fulfil minimum requirements, was conducted with a moderate amount of time, equipment and personnel. The efficiency depends largely on the available channel count. The survey was carried out under different weather conditions that are clearly observable in data quality. The S-wave

propagation responds to the ultra-shallow ground conditions and data quality is better for frozen ground.

Key elements in seismic data analysis were: (1) enhancement of stacking fold and regularization of the data that reduces incoherent noise and ensures equally spaced offset distribution for multi-trace filtering; (2) Component rotation from inline-crossline to radial–transverse coordinates projected large portions of energy from components of an uneven orientation to the same orientation. This resulted in data corresponding to the SV-wave and SH-wave propagation. In these domains, filtering of refracted and surface waves worked better. Both S-wave types could image the sedimentary infill of the Tannwald Basin and show very similar images in the deeper (>50 ms) part, whereas they differ considerably in the upper part. Both types exceed the limits of the previous 2-D P-wave imaging. A detailed interpretation will follow.

It is also noted that 3-D 6-C S-wave surveying gives a benefit compared to 2-D imaging, since we can spatially map geological layers at high fidelity. For future shallow S-wave surveys, we recommend using a one-patch solution if feasible and to account for changing weather conditions during the survey.

ACKNOWLEDGEMENTS

ORCID

Thomas Burschil https://orcid.org/0000-0002-9323-699X
Hermann Buness https://orcid.org/0000-0002-4568-1597
Cedric Schmelzbach
https://orcid.org/0000-0003-1380-8714

REFERENCES

Alford, R.M. (1986) Shear data in the presence of azimuthal anisotropy: Dilley, Texas: 56th Annual International Meeting, SEG, Expanded Abstracts, 476–479.

Anselmetti, F., Preusser, F., Bavec, M., Crouzet, C., Fiebig, M., Gabriel, G. *et al*. (2016) Drilling overdeepened Alpine valleys (DOVE). https://www.icdp-online.org/projects/world/europe/alpine-valleys/details/ [Accessed 22 April 2021].

Bachrach, R. and Nur, A. (1998) High-resolution shallow-seismic experiments in sand. Part I: Water table, fluid flow, and saturation. *Geophysics*, 63(4), 1225–1233.

Brodic, B., Malehmir, A., Bastani, M., Mehta, S., Juhlin, C., Lundberg, E. and Wang, S. (2017) Multi-component digital-based seismic landstreamer and boat-towed radio-magnetotelluric acquisition systems for improved subsurface characterization in the urban environment. *First Break*, 35(8), 41–47.

Brodic, B., Malehmir, A., Pugin, A. and Maries, G. (2018) Three-component seismic land streamer study of an esker architecture through S- and surface-wave imaging. *Geophysics*, 83(6), B339–B353.

Brune, R.H., O'Sullivan, B. and Lu, L. (1994) Comprehensive analysis of marine 3-D bin coverage. *The Leading Edge*, 13(7), 757–762.

Büker, F., Green, A.G. and Horstmeyer, H. (1998) Shallow 3-D seismic reflection surveying: data acquisition and preliminary processing strategies. *Geophysics*, 63(4), 1434–1450.

Büker, F., Green, A.G. and Horstmeyer, H. (2000) 3-D high-resolution reflection seismic imaging of unconsolidated glacial and glacio-lacustrine sediments: processing and interpretation. *Geophysics*, 65(1), 18–34.

Buechi, M.W. (2017) Overdeepened glacial basins as archives for the Quaternary landscape evolution of the Alps: E and G. *Quaternary Science Journal*, 66(1), 3–5.

Buness, H. (2007) Improving the processing of vibroseis data for very shallow high-resolution measurements. *Near Surface Geophysics*, 5(3), 173–182.

Buness, H., Burschil, T. and Tanner, D. (2020) Imaging glacial sediments and tectonics with a small-scale 3-D reflection seismic survey. *26th Conference and Exhibition, EAGE, Extended Abstracts*, 1–4. https://doi.org/10.3997/2214-4609.202020094.

Burschil, T., Buness, H., Tanner, D.C., Wielandt-Schuster, U., Ellwanger, D. and Gabriel, G. (2018) High-resolution reflection seismics reveal the structure and the evolution of the Quaternary glacial Tannwald Basin. *Near Surface Geophysics*, 16(6), 593–610.

Burschil, T., Tanner, D.C., Reitner, J.M., Buness, H. and Gabriel, G. (2019) Unravelling the shape and stratigraphy of a glacially-overdeepened valley with reflection seismic: the Lienz Basin (Austria). *Swiss Journal of Geosciences*, 112(2), 341–355.

Burschil, T. and Buness, H. (2020). S-wave seismic imaging of near-surface sediments using tailored processing strategies. *Journal of Applied Geophysics*, 173, 103927.

Burschil, T., Buness, H., Leineweber, P. and Polom, U. (2021) Results of performance tests of electrodynamic vibratory seismic sources: 27th Near Surface Geoscience Conference and Exhibition. *EAGE, Expanded Abstract*, 1–4.

Chopra, S. and Stewart, R. (2010) Introduction to this special section: multicomponent seismic. *The Leading Edge*, 29(10), 1210–1211.

Clochard, V., DeVault, B.C., Bowen, D., Delépine, N. and Wangkawong, K. (2018) Quadri-joint inversion: method and application to the Big Sky 9C 3D data set in northern, Montana. *Interpretation*, 6(4), SN101–SN118.

Cook, S.J. and Swift, D.A. (2012) Subglacial basins: their origin and importance in glacial systems and landscapes. *Earth-Science Reviews*, 115(4), 332–372.

Cordsen, A., Galbraith, M. and Peirce, J. (2000) *Planning Land 3-D Seismic Surveys*. Houston, TX: Society of Exploration Geophysicists.

Crampin, S. (1985) Evaluation of anisotropy by shear-wave splitting. *Geophysics*, 50(1), 142–152.

Davis, T.L., Terrell, M.J., Benson, R.D., Cardona, R., Kendall, R.R. and Winarsky, R. (2003) Multicomponent seismic characterization and monitoring of the CO 2 flood at Weyburn Field, Saskatchewan. *The Leading Edge*, 22(7), 696–697.

Davogustto Cataldo, O.E., Kwiatkowski, T.J., Marfurt, K.J., Roche, S.L. and Thomas, J.W. (2014) 3D Alford rotation analysis for the diamond M field, midland basin, Texas. *Interpretation*, 2(2), SE63–SE75.

DiSiena, J.P., Gaiser, J.E., Corrigan, D. and Toksöz, M.N. (1984) Horizontal components and shear wave analysis of three-component VSP data. In: Nafi Toksoz, M. and Stewart, R. (Eds.) *Vertical Seismic Profiling, Part B: Advanced Concepts*. Benahavis, Spain: Geophysical Press.

Donati, M., Piazza, J.L., Rollet, A., Baillon, S., Marin, D., Belz, V. *et al*. (2016) 3D-3C multicomponent seismic – a successful fracture characterization case study in Algeria. *First Break*, 34(1). https://doi.org/10.3997/1365-2397.2016001.

Eisenberg-Klein, G., Pruessmann, J., Gierse, G. and Trappe, H. (2008) Noise reduction in 2D and 3D seismic imaging by the CRS method. *The Leading Edge*, 27(2), 258–265.

Ellwanger, D., Wielandt-Schuster, U., Franz, M. and Simon, T. (2011) The Quaternary of the Southwest German Alpine Foreland (Bodensee-Oberschwaben, Baden-Württemberg, Southwest Germany). *Quaternary Science Journal*, 60(2–3), 306–328.

Frei, W., Martin, D. and Baumann, M. (2021) Seismik für den Tiefenbereich bis 2000 m. Swiss Bulletin for Applied Geology, 26(1), 83–94.

Garotta, R. (1999) *Shear Waves from Acquisition to Interpretation*. Houston, TX: Society of Exploration Geophysicists.

Gierse, G., Trappe, H., Pruessmann, J., Eisenberg-Klein, G., Lynch, J. and Clark, D. (2009) Enhanced velocity analysis, binning, gap infill, and imaging of sparse 2D/3D seismic data by CRS techniques. *SEG Technical Program, Expanded Abstracts*, 3279–3283.

Grossman, J.P. and Popov, G. (2014) Case study: 3C and 9C prestack shear wave splitting analysis at Big Sky. *CSEG Recorder*, 39(2), 40–47.

Hardage, B.A., DeAngelo, M.V., Murray, P.E. and Sava, D. (2011) *Multicomponent Seismic Technology*. Houston, TX: Society of Exploration Geophysicists.

Hardage, B.A., Sava, D. and Wagner, D. (2014) SV-P: an ignored seismic mode that has great value for interpreters. *Interpretation*, 2(2), SE17–SE27.

Harris, J.B. (1996) Shear-wave splitting in Quaternary sediments: neotectonic implications in the central New Madrid seismic zone. *Geophysics*, 61(6), 1871–1882.

Hitchings, V.H. and Potters, H. (2000) Production and geologic implications of the Natih 9-C, 3-D seismic survey. *The Leading Edge*, 19(10), 1117–1124.

House, J.R., Boyd, T.M. and Haeni, R.E. (1996) A case study for the acquisition, processing and relevance of 3-D seismic data as applied to the remediation of DNAPL contamination. In: Weimer, P. and Davis, T.L. (Eds.) *Applications of 3-D Seismic Data to Exploration and Production: Geophysical Developments. Series 5*. Houston, TX Society of Exploration Geophysicists, pp. 257–265.

Hubral, P., Höcht, G. and Jäger, R. (1998) An Introduction to the Common Reflection Surface Stack: 60th Conference and Exhibition, *EAGE*, cp-110.

Hunter, J.A., Pullan, S.E., Burns, R.A., Gagne, R.M. and Good, R.L. (1984) Shallow seismic reflection mapping of the overburden-bedrock interface with the engineering seismograph – some simple techniques. *Geophysics*, 49(8), 1381–1385.

Inazaki, T. (2004) High-resolution seismic reflection surveying at paved areas using an S-wave type land streamer. *Exploration Geophysics*, 35(1), 1–6.

Kaiser, A.E., Horstmeyer, H., Green, A.G., Campbell, F.M., Langridge, R.M. and McClymont, A.F. (2011) Detailed images of the shallow Alpine Fault Zone, New Zealand, determined from narrow-azimuth 3D seismic reflection data. *Geophysics*, 76(1), B19–B32.

Krawczyk, C.M., Polom, U. and Beilecke, T. (2013) Shear-wave reflection seismics as a valuable tool for near-surface urban applications. *The Leading Edge*, 32(3), 256–263.

Lang, J., Winsemann, J., Steinmetz, D., Polom, U., Pollok, L., Böhner, U. *et al*. (2012) The Pleistocene of Schöningen, Germany: a complex tunnel valley fill revealed from 3D subsurface modelling and shear wave seismics. *Quaternary Science Reviews*, 39, 86–105.

Lundberg, E., Malehmir, A., Juhlin, C., Bastani, M. and Andersson, M. (2014) High-resolution 3D reflection seismic investigation over a quick-clay landslide scar in southwest Sweden. *Geophysics*, 79(2) B97–B107.

Mari, J.L. and Porel, G. (2008) 3D seismic imaging of a near-surface heterogeneous aquifer: a case study. *Oil and Gas Science and Technology-Rev. IFP*, 63(2), 179–202.

Pan, Y., Gao, L. and Bohlen, T. (2021) Random-objective waveform inversion of 3D-9C shallow-seismic field data. *Journal of Geophysical Research: Solid Earth*, 126(9), e2021JB022036. https://doi.org/10.1029/2021JB022036

Pan, Y., Xia, J., Xu, Y. and Gao, L. (2016) Multichannel analysis of Love waves in a 3D seismic acquisition system. *Geophysics*, 81(5), EN67–EN74.

Polom, U., Alrshdan, H., Al-Halbouni, D., Holohan, E.P., Dahm, T., Sawarieh, A. *et al*. (2018) Shear wave reflection seismic yields subsurface dissolution and subrosion patterns: application to the Ghor Al-Haditha sinkhole site, Dead Sea, Jordan. *Solid Earth*, 9, 1079–1098.

Polom, U., Druivenga, G., Grossmann, E., Grüneberg, S. and Rode, W. (2011) Transportabler Scherwellenvibrator: Deutsches Patent und Markenamt. Patentschrift DE10327757B4.

Potters, J.H.H.M., Groenendaal, H.J.J., Oates, S.J., Hake, J.H. and Kalden, A.B. (1999) The 3D shear experiment over the Natih field in Oman: reservoir geology, data acquisition and anisotropy analysis. *Geophysical Prospecting*, 47(5), 637–662.

Pugin, A. and Yilmaz, Ö. (2017) There is no pure P-or S-wave land seismic source. *SEG Technical Program, Expanded Abstracts*, 5162–5166.

Pugin, A. and Yilmaz, Ö. (2019) Optimum source-receiver orientations to capture PP, PS, SP, and SS reflected wave modes. *The Leading Edge*, 38(1), 45–52.

Pugin, A.J.M., Pullan, S.E. and Hunter, J.A. (2009) Multicomponent high-resolution seismic reflection profiling. *The Leading Edge*, 28(10), 1248–1261.

Pugin, A.M., Brewer, K., Cartwright, T., Pullan, S.E., Perret, D., Crow, H. and Hunter, J.A. (2013) Near surface S-wave seismic reflection profiling – new approaches and insights. *First Break*, 31(2). https://doi.org/10.3997/1365-2397.2013005.

Sargent, C. and Goulty, N.R. (2007) Seismic reflection investigation of gypsum dissolution and subsidence at Hell Kettles, Darlington: 69th Conference and Exhibition incorporating SPE EUROPEC 2007, EAGE, cp-27.

Schmelzbach, C., Horstmeyer, H. and Juhlin, C. (2007) Shallow 3D seismic-reflection imaging of fracture zones in crystalline rock. *Geophysics*, 72(6), B149–B160.

Schmelzbach, C., Reiser, F., Sollberger, D., Rabenstein, L., Horstmeyer, H., Sutter, E. *et al*. (2014) Multi-method geophysical imaging of a Quaternary valley in northern Switzerland. *SEG Technical Program, Expanded Abstracts*, 2083–2087.

Schmelzbach, C., Sollberger, D., Greenhalgh, S.A., Horstmeyer, H., Maurer, H. and Robertsson, J.O.A. (2016) 9C seismic data acquisition for near-surface applications: recording, waveform reciprocity and 4C rotation: 78th Conference and Exhibition, EAGE, Conference Proceedings, 1–5. https://doi.org/10.3997/2214-4609.201601639.

Sheriff, R.E. and Geldart, L.P. (1995) *Exploration Seismology*. Cambridge: Cambridge University Press.

Shuck, E.L., Davis, T.L. and Benson, R.D. (1996) Multicomponent 3-D characterization of a coalbed methane reservoir. *Geophysics*, 61(2), 315–330.

Simmons, J. and Backus, M. (1999a) Radial-transverse (SV-SH) coordinates for 9-C 3-D seismic reflection data analysis. *SEG Technical Program, Expanded Abstracts*, 728–731.

Simmons, J. and Backus, M. (1999b) Shear-wave splitting: Tutorial, issues and implications for 9-C 3-D seismic reflection data. *SEG Technical Program, Expanded Abstracts*, 788–791.

Simmons, J. and Backus, M. (2001) Shear waves from 3-D–9-C seismic reflection data: have we been looking for signal in all the wrong places? *The Leading Edge*, 20(6), 604–612.

Simmons, J., Backus, M.M., Hardage, B.A. and Graebner, R.J. (1999) Case history: 3-D shear-wave processing and interpretation in radial-transverse (SV-SH) coordinates. *SEG Technical Program, Expanded Abstracts*, 792–795.

Sloan, S.D., Steeples, D.W. and Tsoflias, G.P. (2009) Ultra-shallow imaging using 3D seismic-reflection methods. *Near Surface Geophysics*, 7(5–6) 307–314.

Souza, T., Barros, T. and Lopes, R. (2019) Application of the CO-CRS method for seismic data regularization. *16th International Congress of the Brazilian Geophysical Society, SBGf*, 1–6.

Spitzer, R., Nitsche, F.O., Green, A.G. and Horstmeyer, H. (2003) Efficient acquisition, processing, and interpretation strategy for shallow 3D seismic surveying: A case study. *Geophysics*, 68(6), 1792–1806.

Vermeer, G.J. (2010) 3D symmetric sampling of sparse acquisition geometries. *Geophysics*, 75(6), WB3–WB14.

Wadas, S.H., Polom, U. and Krawczyk, C.M. (2016) High-resolution shear-wave seismic reflection as a tool to image near-surface subrosion structures–a case study in Bad Frankenhausen, Germany. *Solid Earth*, 7(5), 1491–1508.

Yilmaz, Ö. (2001) *Seismic Data Analysis*. Houston, TX: Society of Exploration Geophysicists.